Isospin diffusion in binary collisions of $^{32}S + ^{40,48}Ca$ and $^{32}S + ^{48}Ti$ at 17.7 MeV/nucleon

S. Piantelli,[1,*] S. Valdré,[1] S. Barlini,[1,2] G. Casini,[1] M. Colonna,[3] G. Baiocco,[4] M. Bini,[1,2] M. Bruno,[5,6] A. Camaiani,[1,2] S. Carboni,[1,2] M. Cicerchia,[7,8] M. Cinausero,[7] M. D'Agostino,[5,6] M. Degerlier,[9] D. Fabris,[10] N. Gelli,[1] F. Gramegna,[7] D. Gruyer,[1,†] V. L. Kravchuk,[11] J. Mabiala,[7] T. Marchi,[12] L. Morelli,[5,6] A. Olmi,[1] P. Ottanelli,[1,2] G. Pasquali,[1,2] and G. Pastore[1,2]

[1]*INFN sezione di Firenze, I-50019 Sesto Fiorentino, Italy*
[2]*Dipartimento di Fisica, Università di Firenze, I-50019 Sesto Fiorentino, Italy*
[3]*INFN, Laboratori Nazionali del Sud, I-95123 Catania, Italy*
[4]*Dipartimento di Fisica, Università di Pavia, I-27100 Pavia, Italy*
[5]*Dipartimento di Fisica e Astronomia, Università di Bologna, I-40127 Bologna, Italy*
[6]*INFN sezione di Bologna, I-40127 Bologna, Italy*
[7]*INFN, Laboratori Nazionali di Legnaro, I-35020 Legnaro, Italy*
[8]*Dipartimento di Fisica, Università di Padova, I-35131 Padova, Italy*
[9]*Nevsehir Haci Bektas Veli University, Science and Art Faculty, Physics Department, Turkey*
[10]*INFN, Sezione di Padova, I-35131 Padova, Italy*
[11]*National Research Centre "Kurchatov Institute", 123182 Moscow, Russia*
[12]*Institute for Nuclear and Radiation Physics, KU Leuven, B-3001 Leuven, Belgium*

(Received 11 January 2017; revised manuscript received 7 July 2017; published 27 September 2017)

The systems $^{32}S + ^{40,48}Ca$ and $^{32}S + ^{48}Ti$ at 17.7 MeV/nucleon were investigated with the setup general array for fragment identification and for emitted light particles in dissipative collisions (GARFIELD) plus ring counter (RCo) at Laboratori Nazionali di Legnaro (LNL) of Istituto Nazionale di Fisica Nucleare (INFN). Fusion evaporation (FE), fusion fission (FF), and deep inelastic (DIC) events were identified, also through the comparison with the prediction of a transport model (stochastic mean field, SMF), coupled to GEMINI++ as an afterburner. This work mainly deals with the study of isospin transport phenomena in DIC events. In particular, the isospin diffusion is highlighted by comparing the average isotopic content of the quasiprojectile (QP) remnants observed when the target is the $N = Z$ nucleus ^{40}Ca and when it is the neutron-rich ^{48}Ca. Also, the d/p and t/p ratios for particles forward emitted with respect to the QP were found to increase with increasing N/Z of the target.

DOI: 10.1103/PhysRevC.96.034622

I. INTRODUCTION

It is well known that heavy-ion reactions at beam energies around 20 MeV/nucleon represent a very interesting case where mean-field-driven phenomena coexist with effects due to nucleon-nucleon collisions.

At these energies, the reaction cross section is mainly shared among fusion-evaporation (FE) or fusion-fission (FF) events and deep inelastic collisions (DIC). Pre-equilibrium emission may be not negligible, as shown, for example, in Refs. [1,2], producing a high-energy tail in the energy spectra of the emitted light charged particles with respect to the Maxwellian shape expected for a pure evaporative emission. When the reaction partners have different N/Z, effects of *isospin diffusion*, which push toward the N/Z equilibration of quasiprojectile (QP) and quasitarget (QT) [3], are expected. Such effects are driven by the isospin[1] gradient between the two colliding nuclei and depend on the symmetry energy term of the nuclear equation of state (EOS). This subject has been studied for decades and there are many examples in the literature [4–17] describing the charge equilibration details in different energy regimes, from slightly above the Coulomb barrier [9,11] up to the Fermi energies [5,14–17]. In a number of cases, the process has been analyzed, for a given system, as a function of the dissipation associating its evolution with the reaction time scales. In old experiments, the focus was mainly on linking the N/Z equilibration to the microscopic process of energy dissipation via nucleon exchanges [4]. Typically, the evolution of the Z, A distributions for identified QP was followed and connected to the proton or neutron fluxes developing during the nuclear interaction. Indeed, this strict connection between energy damping and nucleon transfer is at the origin of the term multinucleon-transfer (MNT), used to indicate these collisions. This acronym commonly refers to collisions at rather large impact parameters, bridging the direct reactions (one or two transfers only) to the strongly dissipative collisions, where the picture of individual transfers of a few nucleons across a "window" loses validity. On the other hand, MNT has a large relevance as a method to produce exotic nuclei at moderate excitation energies. At present, this possibility is even reinforced thanks to the use of radioactive beams: MNT represents a powerful method for γ spectroscopy because one can study the nuclear structure of nuclei toward the nuclear drip lines [8–11]. In some old works [5,6], where projectile-like fragments were isotopically identified, an attempt was made to characterize both direct

*Corresponding author: silvia.piantelli@fi.infn.it
†Present address: Normandie Univ, ENSICAEN, UNICAEN, CNRS/IN2P3, LPC Caen, 14000 Caen, France.

[1]As usually done in this field, the word *isospin* does not indicate the third component of the isotopic spin, but the ratio N/Z, related to the neutron-proton imbalance.

and dissipative (and hence also MNT) collisions in mass-asymmetric systems in direct kinematics. At low bombarding energies, they observed a dominance of direct reactions (with nucleon transfers favoring a net mass gain of the heavy target), while the deep-inelastic component (which produced hot quasiprojectiles) progressively increased with increasing bombarding energy from 9 to 22 MeV/nucleon. However, the subject of charge equilibration was only marginally addressed when discussing the relative weight of direct vs deep-inelastic collisions and no specific point was done about the dependence on the centrality of the collisions. More recently, isospin effects were investigated from a different perspective. The focus was on the link between the isospin dynamics and the nuclear EOS and, in particular, its symmetry energy term. This aspect motivated a series of experiments mainly at Fermi energies [14,16–18] with large-acceptance multidetectors but also below 20 MeV/nucleon, often using spectrometers. Just as an example, in a recent study [12] the isotopic distribution of the QP coming from a ^{86}Kr beam at 15 MeV/nucleon was measured by means of the momentum achromat recoil spectrometer (MARS) [19]. The authors found that when the target is ^{124}Sn, the isotopic composition of the QP is shifted to the neutron-rich side with respect to the case of the neutron-deficient ^{112}Sn. In the Fermi energy regime (beam energy in the range ∼20–50 MeV/nucleon), besides the isospin diffusion process [15], one expects also *isospin drift* effects, driven by the density gradient and depending on the derivative of the symmetry energy. Such effects produce a neutron enrichment of the more dilute neck zone with respect to the QP and QT region at normal density [17,18]. This is not the case at the lower energies considered in this work, because the whole system remains close to the normal density during the reaction. However, also at lower energies one cannot exclude the possibility that some surface effects [13] or the occurrence of very elongated shapes [20] may produce some density gradient, thus triggering the isospin drift mechanism [21]. For example, it was shown that for the system ^{58}Ni + ^{24}Mg at 11 MeV/nucleon [20] the shape of the α-particle spectra in FE events can be reproduced by the statistical model only assuming the "initial formation of a highly deformed composite system, or alternatively a dinuclear system, composed of the two highly excited incoming nuclei, which later in the cascade revert to a more conventionally shaped compound nucleus" (p. 2454). In Ref. [13], the isotopic distribution of the QP for reactions involving a medium-mass projectile (^{64}Ni) and a heavy target (^{208}Pb) at beam energy lower than 10 MeV/nucleon could be well reproduced by a nucleon exchange model only introducing an extended nuclear density profile; the effect seems to disappear when the beam energy increases up to 25 MeV/nucleon. An example of a system around the lower limit of the Fermi regime showing both the isospin diffusion and the isospin drift phenomena is presented in Ref. [14] for the reactions ^{40}Ca + ^{40,48}Ca at 25 MeV/nucleon. Looking at the isobaric ratio ^{7}Li/^{7}Be for the symmetric system ^{40}Ca + ^{40}Ca, the authors found that midvelocity emitted fragments show a higher isobaric ratio than those emitted by the QP. Moreover, for QP emitted fragments the ratio ^{7}Li/^{7}Be is higher when the target is the n-rich ^{48}Ca.

From a theoretical point of view, although a perfect description is still lacking, a rather good reproduction of the charge equilibration process in heavy-ion collisions was obtained with nucleon exchange models (see Ref. [7] for a comprehensive overview). The main idea of these models is that successive exchanges of nucleons between the two nuclei are responsible for the main features of dissipative binary collisions, like large excitation energies, high spins, and excitation of collective modes. In the cited paper [7], a detailed summary was done about the knowledge of isospin equilibration at that time, underlining the existing problems, both on the experimental and theoretical side. The authors pointed to various critical aspects that made it difficult to draw clean conclusions; for instance, the important role of evaporation and pre-equilibrium emissions in determining the final experimental distributions. Moreover, the authors warned that erroneous conclusions can be drawn when data are collected in too narrow phase-space regions of the reaction products. As a general recommendation, the authors suggested to use both measurements with efficient detectors and MonteCarlo approaches that allow one to perturb the model predictions event by event with all known physical or experimental effects (e.g., evaporation of particles, thresholds, and identification limits).

Following this strategy, we present here a study on the isospin diffusion using a well-performing detector and a full Monte Carlo package, including a modern nuclear transport model (to produce primary distributions) coupled with a renowned sequential decay code (to cool down the primary nuclei) and also routines to mimic all known experimental distorsions and resolutions. In fact, a good reproduction of the main characteristics of the collisions can be obtained by means of transport models, such as the stochastic mean field (SMF) [3,22]. These models include the mean field contribution, described by means of a phenomenological interaction (e.g., a Skyrme interaction [23]), the collisional integral, which takes into account on average nucleon-nucleon collisions, and a fluctuation term. The adopted mean field Hamiltonian is linked to the nuclear EOS, which, in the case of asymmetric nuclear matter, is not well known far from normal density, and different parametrizations (generally indicated as asystiff and asysoft) can be adopted [24].

This work presents the results of an experimental investigation of the reactions ^{32}S + ^{40,48}Ca and ^{32}S + ^{48}Ti at 17.7 MeV/nucleon; the experiment was performed at the Laboratori Nazionali di Legnaro (LNL) of INFN (Italy) with the GARFIELD plus ring counter (RCo) setup [25], whose high angular coverage and relatively low thresholds allow for the detection of the main reaction channels, such as FE, FF, and DIC. In particular, this work deals with the isospin diffusion in DIC, which was highlighted by looking at the average isospin ($\langle N\rangle/Z$) of the QP, thanks to the good isotopic resolution of the RCo. A clear effect of $\langle N\rangle/Z$ enrichment of the QP was observed when the target was the neutron-rich ^{48}Ca. It was associated with a simultaneous increase of the d/p and t/p ratios for particles forward emitted with respect to the QP as compared with the isospin-symmetric reaction ^{32}S + ^{40}Ca. To our knowledge, in literature there are no other direct experimental evidences of isospin enrichment of the QP for nearly symmetric systems at the same time as light

as ours and at energies similar to that of the present study. In fact, experimental studies on the charge equilibration in medium-mass systems are rather rare, especially at bombarding energies bridging the Coulomb barrier region and the Fermi domain. As a matter of fact, most works reported in the old review papers [7] are on collisions well below 10 MeV/nucleon. Moreover, as remarked above, here we attempt a comprehensive description of the reaction mechanisms using an efficient detector and interpreting the data under the guide of a modern transport model. This model is capable of describing the complexity of the nuclear reaction from peripheral to central collisions and, in this context, to explore the particular subject of isospin equilibration.

This paper is organized as follows: The main characteristics of the setup are recalled in Sec. II; the model and the event-sorting procedure are shown in Sec. III; the results concerning the isospin diffusion process in the DIC channel are presented and discussed in Sec. IV both for experimental and simulated data, while the main conclusions are summarized in Sec. V.

II. EXPERIMENTAL SETUP

A pulsed beam of ^{32}S at 17.7 MeV/nucleon with repetition period of 200 ns and average current of 0.1 pnA was delivered by the ALPI linear accelerator of Laboratori Nazionali di Legnaro (LNL) of INFN (Italy). During the experiment ^{40}Ca and ^{48}Ca targets with 500 μg/cm^2 thickness and a ^{48}Ti target with a thickness of 600 μg/cm^2 were used as main targets of the experiment. The Ca targets were sandwiched with two thin layers of ^{12}C (10 μg/cm^2 on both sides) in order to prevent the prompt oxidation process. Therefore, also a ^{12}C target with a thickness of 15 μg/cm^2 was employed for a short measurement in order to evaluate the background due to nuclear reactions on C.

The experimental setup consisted of the GARFIELD plus RCo detectors, extensively described in Ref. [25], covering 66% of the whole solid angle and 72% of the forward hemisphere in the present experiment. Here only the main characteristics will be recalled, referring to Fig. 1 of Ref. [25].

GARFIELD consists of 96 telescopes (gas drift chamber as ΔE stage and CsI(Tl) as $E_{\rm res}$ stage) at forward angles (between 30° and 85°) and 84 CsI(Tl) scintillators covering the angles between 95° and 150°. The azimuthal coverage of each detection unit is 15°, for a total of 24 and 21 sectors at forward and backward angles, respectively. The CsI(Tl) scintillators are grouped in 8 polar rings and their polar coverage increases from 10.5° to 14.5° moving away from the beam direction. In the backward hemisphere, an azimuthal region 45° wide is left free to possibly accommodate ancillary detectors, such as γ detectors, although not during the measurement discussed in this work. The drift chamber at forward angles consists of a unique gas volume, filled with flowing CF_4 at a pressure of about 50 mbar;[2] each azimuthal sector is equipped with a glass microstrip electrode, which produces sizable signals even for weakly ionizing particles (such as α particles), thanks to a moderate charge carrier multiplication. Each $\Delta E-E$ telescope is obtained coupling the signal of a microstrip electrode to that of a CsI(Tl) and it allows to identify fragments up to $Z = 16$ (without isotopic resolution), provided that they reach the CsI(Tl) detectors. The CsI(Tl) scintillators are read out by photodiodes and they are all equipped with digital electronics. They are able to identify hydrogen and helium isotopes via the standard fast vs slow technique for CsI(Tl) scintillators.

The RCo is a three-layer detector covering polar angles between 5.4° and 17.0° with azimuthal symmetry. The first layer consists of an ionization chamber (IC) with a single gas volume filled with flowing CF_4 at a pressure of 50 mbar. The ionization chamber is segmented in 8 sectors. For each sector, 8 reverse-mounted silicon strip detectors with a thickness of about 300 μm are located behind the IC, followed by 6 CsI scintillators read out by photodiodes. All these detectors are equipped with digital electronics. During the measurement, the most forward Si strips (polar angles between 5.4° and 7.2°) were covered by a metallic shield in order to avoid damaging the strips by elastic scattering. Particle identification can be obtained exploiting four different correlations. First of all, IC vs silicon strips is used for the identification of heavy ions with low kinetic energy; unitary charge resolution is obtained up to $Z \sim 30$ (which is enough for the evaporation residues, as it will be shown in the following section). For heavier ions, unitary charge resolution is not possible. Ions with range greater than a given threshold (more than 30 μm and increasing with the charge of the ion, see Ref. [26]) are identified in Si strips with the PSA technique, using the correlation energy vs charge rise time. For our reaction, only ions up to the charge of the projectile ($Z = 16$) can be identified by means of this technique. When the ions punch through the silicon layer and reach the CsI(Tl) scintillators, isotopic resolution (up to $Z = 14$ in our experiment) is obtained with the $\Delta E - E$ technique. This capability is crucial for the present work, which deals with the isotopic distributions. Finally, fast light particles ($Z = 1,2$) can be isotopically identified by means of the PSA method in CsI(Tl). An example of the obtained

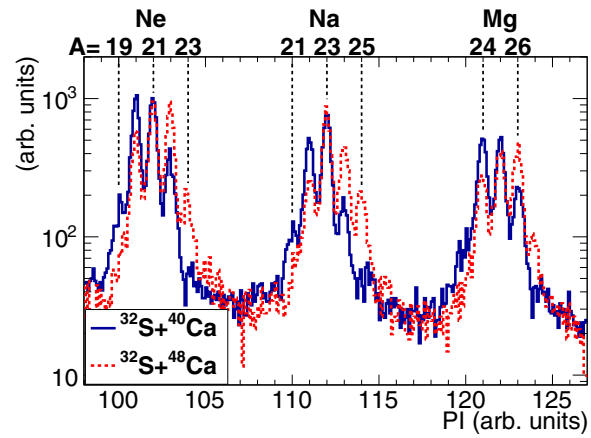

FIG. 1. Particle identification (PI) spectrum obtained from the Si-Csi(Tl) correlation of a typical telescope of RCo. Continuous line: ^{32}S + ^{40}Ca system; red dotted line: ^{32}S + ^{48}Ca system. Spectra are normalized to the same integral. In the upper part of the plot, the mass numbers corresponding to some identified isotopes are shown.

[2] A second gas drift chamber is located at backward angles, but since its gas pressure is 20 mbar only, it cannot be used as ΔE stage.

isotopic resolution from Si-CsI(Tl) correlations is shown in Fig. 1 for a typical telescope; the Ne-Mg region is expanded. The continuous curve corresponds to the system $^{32}S + ^{40}Ca$, while the dotted curve corresponds to the reaction with the neutron-rich target ^{48}Ca. This plot shows that, as expected, in the ^{48}Ca case the inclusive isotopic distribution (without any selection of the reaction mechanism) is clearly shifted towards the neutron rich side.

III. DATA ANALYSIS

A. Characteristics of the reactions

The main characteristics of the studied reactions (excitation energy per nucleon, grazing parameters, N/Z ratio, etc.) are summarized in Table I. The theoretical excitation energy per nucleon in case of complete fusion is similar for the three reactions. The N/Z of the projectile (^{32}S in all cases) is equal to 1.00, while for the targets it spans a range between 1.00 and 1.40. As a consequence, from the point of view of the isospin diffusion, the system $^{32}S + ^{40}Ca$ should not show any effect, because the system is balanced in N/Z, although the reaction is not mass symmetric. The effect of isospin diffusion should be more and more pronounced moving to ^{48}Ti ($N/Z = 1.18$) and to ^{48}Ca ($N/Z = 1.40$). The grazing angle, quite similar for all the reactions, is such that, due to the angular coverage of the setup, peripheral collisions are partially suppressed. Moreover, this class of reactions is further reduced by the adopted experimental trigger (at least one particle detected in GARFIELD and one particle detected in RCo).

Table I includes l_{graz} and $l^{Bf=0}_{Sierk}$, which are the grazing angular momentum and the critical angular momentum beyond which the fission barrier vanishes (i.e., the CN cannot be formed, because the system is unstable against instantaneous fission), calculated according to the Sierk model [27]. From the comparison of these values, it is clear that, besides fusion events (FE or FF), deep inelastic collisions take place in considerable amount. The selection of the different channels is a quite challenging task, due to their partial superposition in all the experimental observables. As a consequence, we relied on a well-performing transport model, the SMF model [22] (implemented in the TWINGO code [29]), coupled to the statistical model (implemented in the GEMINI++ code [30]) as afterburner, in order to identify the best selection criteria on the various observables to separate the different event classes. This model is able to reproduce the main characteristics of dissipative events. The description of the most peripheral reactions would require a higher accuracy, but the latter events, in our case, are experimentally strongly suppressed and can be neglected here.

B. The model: TWINGO plus GEMINI++

Low-energy heavy-ion reactions are governed, to a large extent, by one-body dissipation mechanisms. The main reaction path ranges from (incomplete) fusion to binary exit channels, such as deep-inelastic or quasifission processes. The characterization of the reaction dynamics is commonly provided by microscopic transport approaches (e.g., Refs. [22,31–35]) or more macroscopic models, describing the behavior of selected degrees of freedom (e.g., Refs. [36–40]). Based on the use of nuclear effective interactions, complemented by the suitable parametrizations of the two-body nucleon cross section, transport theories have the advantage to represent, in a consistent way, the time evolution of the nucleon one-body density in response to the action of mean field and two-body dissipation. Pre-equilibrium effects are automatically taken into account along the reaction dynamics and fluctuation terms, related to the stochastic nature of nucleon-nucleon collisions, are introduced at several levels of accuracy [22,41]. On the other hand, macroscopic models only deals with the evolution of suitable quantities (such as multipole moments, charge/mass asymmetries). This allows one to obtain a quite accurate description of fluctuations, which is based on the solution of the Langevin equation, reproducing quasifission events and fusion-fission dynamics [37,40]. Here we are mainly interested in (incomplete) fusion and deep inelastic events. Thus we will adopt the SMF transport model, which incorporates pre-equilibrium effects and has proven to give an appropriate description of low and Fermi energy reactions [18,21]. The TWINGO model is described in detail elsewhere [22]; here we recall only the main characteristics, which have an impact on the comparison with the experimental data. In order to simulate the evolution of the one-body distribution function, taking into account also the fluctuations, each nucleon is replaced by a set of test particles (50 test particles per nucleon, in our case); the test particles are placed in a space lattice in which they are subject to a mean field of Skyrme type [23]. In our case, the space lattice, divided into cubic cells with a volume of 1 fm^3, has a size of $40 \times 40 \times 120$ fm^3 (with the larger size along the beam axis). The evolution of the distribution function takes place according to the Boltzmann-Nordheim-Vlasov (BNV) transport equation [42], including also a collisional

TABLE I. Main reaction parameters. $(N/Z)^{system}$, $(N/Z)^{proj}$, and $(N/Z)^{target}$ are the isospin of the total system, of the projectile, and of the target, respectively. E^*/A is the excitation energy per nucleon in case of complete fusion. CN is the primary compound nucleus formed in case of complete fusion. ϑ_{graz} and l_{graz} are the grazing angle and the grazing angular momentum, respectively. $l^{Bf=0}_{Sierk}$ is the critical angular momentum beyond which the fission barrier vanishes, calculated according to Ref, [27]. σ_R is the total reaction cross section evaluated according to Ref. [28].

Reaction	$(N/Z)^{system}$	$(N/Z)^{proj}$	$(N/Z)^{target}$	E^*/A (MeV/nucleon)	CN	ϑ_{graz} (deg)	l_{graz} ($\hbar$)	$l^{Bf=0}_{Sierk}$ ($\hbar$)	σ_R (barn)
$^{32}S + ^{40}Ca$	1.00	1.00	1.00	4.25	^{72}Kr	5.13	142	52.1	2.37
$^{32}S + ^{48}Ti$	1.11	1.00	1.18	4.17	^{80}Sr	5.47	157	60.2	2.49
$^{32}S + ^{48}Ca$	1.22	1.00	1.40	4.32	^{80}Kr	4.92	158	63.0	2.53

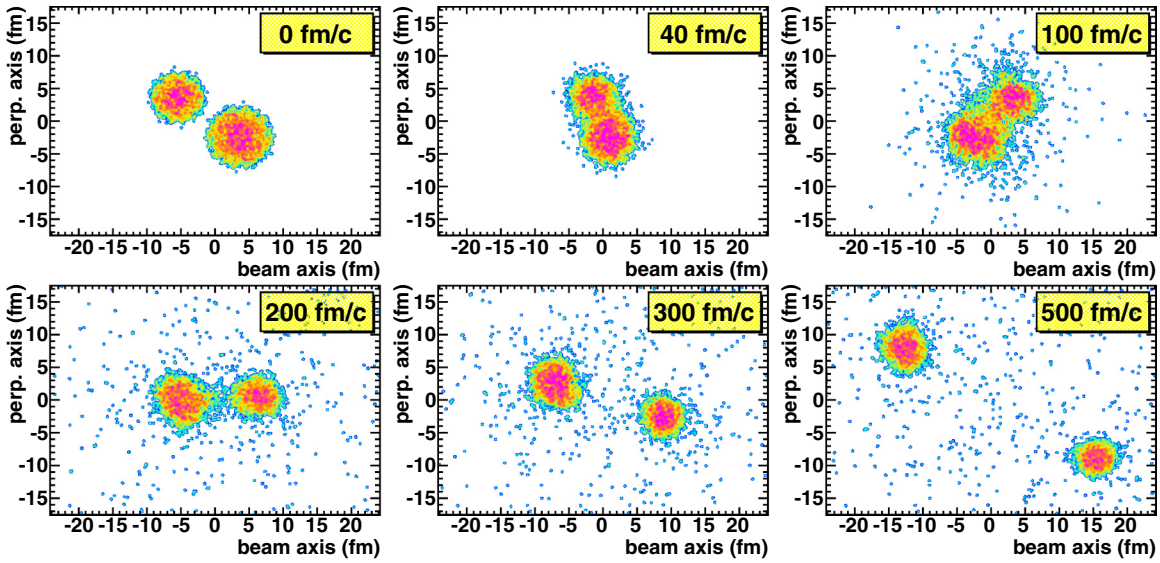

FIG. 2. Event produced by TWINGO with $b = 5.8$ fm for the reaction $^{32}S + ^{48}Ca$. Each picture represents a screenshot of the system at a given time. Each point represents the position of a test particle.

term and a stochastic term (projected in coordinate space), the latter simulating the fluctuations with respect to the average evolution. For each event, at the end of the dynamical calculation a coalescence algorithm [29] is applied to the one-body density $\rho(r)$, which connects neighboring cells with density larger than 0.03 fm^{-3} in order to find the primary fragments, which are then fed to the afterburner code. The choice of the time at which one stops the calculation and applies the coalescence algorithm (generally chosen as the time when the average multiplicity of primary fragments saturates) is crucial. This can be understood by looking at Fig. 2, where an event produced by TWINGO for the reaction $^{32}S + ^{48}Ca$ with impact parameter $b = 5.8$ fm (a zone of centrality where both binary and fusion events can take place, see Fig. 3) is shown as a function of time. Each picture is a screenshot of the system at a given time and each point on the pictures represents the position of a single test particle. The calculation

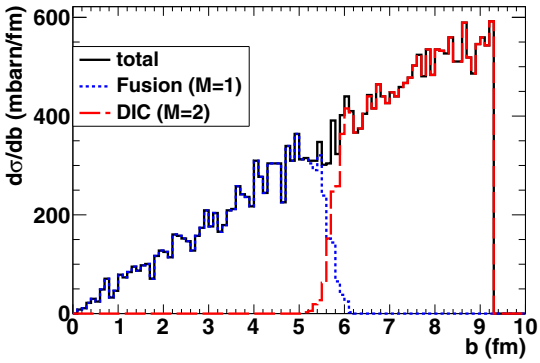

FIG. 3. Continuous black line: impact parameter distribution given as input to TWINGO; the binning of the abscissa is 0.1 fm. Dotted blue line (coincident with the black one below 5 fm): impact parameter distribution associated with fusion events. Dashed red line: impact parameter distribution associated with DIC events. The coalescence algorithm was applied at 300 fm/c.

has to be stopped after the exit channel can be clearly identified. In fact, if we stop the calculation too early (for example, at 200 fm/c for the event of Fig. 2), a clearly eventual binary event can be erroneously classified as a fusion event: Due to the bridge of test particles still connecting the two main fragments, the coalescence algorithm recognizes them as a unique big fragment, without caring for its deformation. On the other side, during the time evolution the system emits test particles, either as pre-equilibrium emission or as evaporative decay. As a consequence, the more the calculation goes on and the coalescence procedure is delayed, the more the excitation energy of the fragments fed to the afterburner is reduced. In principle, this fact should not be an issue because this only means that part of the secondary decay is directly demanded to the dynamical model rather than to the afterburner. The problem arises from the fact that, as a general limitation of mean field models, TWINGO only emits nucleons (by the way, in the present version of the code, not included in the final set of data fed to the software replica of the setup), being unable to produce light complex particles. Within the model, we consequently investigated the most reasonable time to stop the dynamical stage (in the range 200–500 fm/c), finally choosing the value 300 fm/c as the shortest time for the proper fragment identification in all kind of events.

We produced 10^4 events for each system, covering the whole range of impact parameters up to grazing collisions, according to a triangular distribution (black continuous line labeled as "total" in Fig. 3). Then, after propagating the fragments along Coulomb trajectories up to 1200 fm/c (in order to properly boost the velocity of the fragments as in the experimental case), we applied GEMINI++ as afterburner, producing 2×10^3 secondary events for each primary event of TWINGO. The simulated events were then filtered with a software replica of the experimental setup (geometrical coverage, resolutions, and identification thresholds) in order to be able to compare them with the experimental data. We tested also two different parametrizations for the symmetry

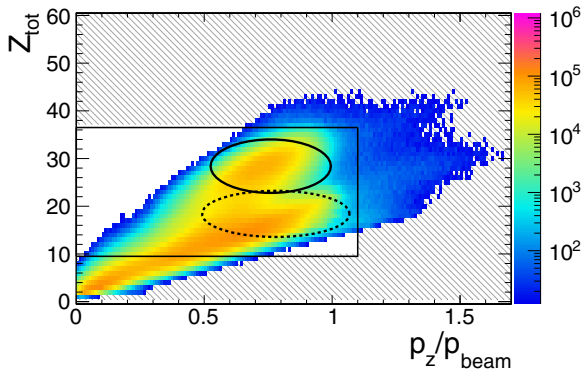

FIG. 4. Experimental data: distribution of events as a function of total detected charge and total momentum along the beam axis, normalized to the beam value, for the system $^{32}S + ^{48}Ca$. The hatched area represents the region of events excluded in the analysis. The area inside the continuous ellipse corresponds mainly to fusion events, while the area inside the dotted ellipse includes incomplete DIC (where only the QP is detected) or incomplete FF events (where only one fission fragment is detected).

term of the EOS: an asystiff and an asysoft [24] one; all the shown pictures refer to the asysoft case, unless explicitly noted otherwise.

As expected, TWINGO predicts two classes of primary events: incomplete fusion events (with fragment multiplicity $M = 1$ after the coalescence algorithm) and DIC events ($M = 2$), as shown in Fig. 3, where the impact parameter distributions associated with fusion events (dotted blue line) and with DIC events (dashed red line) are plotted. DIC events occur from peripheral collisions down to b around 5 fm; on the contrary, fusion events dominate at low impact parameters with a tail up to 6 fm. As a consequence, there is a narrow region of impact parameters where both event classes overlap and thus the pouring from one class to the other, depending on the coalescence time, can be significant. Obviously, after applying the afterburner, part of the fusion events will end up in fusion-fission events, with two heavy fragments in the exit channel, similar to what happens in DIC events. This effect, which takes place also in the experimental case, coupled to the fact that often only one fragment of a binary event is experimentally detected because of the geometrical cuts and identification thresholds, introduces uncertainties in the experimental classification of the events, as it has been pointed out, e.g., in Ref. [43].

C. Event sorting

Concerning the experimental data, Fig. 4 shows the correlation between the total detected charge (Z_{tot}) and the total momentum along the beam axis, normalized to the beam value (p_Z/p_{beam}), for the system $^{32}S + ^{48}Ca$. The events inside the hatched area are rejected in the analysis (and they are not included in all the following figures), because those below $Z_{tot} = 10$ correspond to events in which only light particles are collected (10% of the total events for the ^{48}Ca case and 13% of the total events for the ^{40}Ca case) and the events with $Z_{tot} > 36$ and $p_Z/p_{beam} > 1.1$ are badly detected events (0.1% of the total events for both systems). In the accepted region, two main zones can be identified: the upper one (inside the continuous ellipse), at higher Z_{tot}, mainly corresponds to fusion events (FE or FF), while the lower one (inside the dotted ellipse) mostly corresponds to DIC events in which only the QP is detected (or to FF events where one of the fission fragments is lost). In Fig. 5, the experimental [Fig. 5(a)] and simulated [Fig. 5(b)] correlations between the charge of fragments (with $Z \geqslant 3$) and their velocity in the center of mass (c.m.) are presented for the system $^{32}S + ^{48}Ca$. Simulated data have been filtered by means of a software replica of the experimental setup.

The evaporation residues ER of FE events can be easily recognized in the spot at low c.m. velocity and high Z; their charge and velocity distributions are broader in the experimental case than in the simulated one. FF and DIC events are mixed in the region at velocities above 15 mm/ns. By comparing Figs. 5(a) and 5(b), we can evince that the general characteristics of the experimental correlation are reproduced by the simulation. As a consequence, we can conclude that we can trust the model to tune the criteria we need to apply for separating the different event classes.

A sufficiently clean separation among the different channels can be obtained exploiting the correlation between the total detected charge Z_{tot} and the flow angle ϑ_{flow} (see Ref. [44] and references therein). The flow angle, which is commonly used to classify the events in experiments with large angular coverage, is obtained from the diagonalization of the c.m. momentum

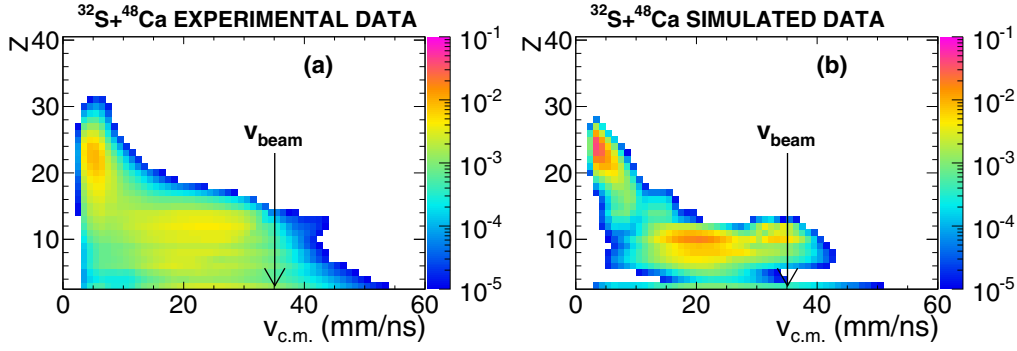

FIG. 5. Yields as a function of the charge Z and the c.m. velocity for all the fragments with $Z \geqslant 3$ for the reaction $^{32}S + ^{48}Ca$. Distributions are normalized to unitary integral. (a) Experimental data; events belonging to the hatched area of Fig. 4 are not included. (b) Simulated events produced by TWINGO followed by GEMINI++, filtered by means of a software replica of the detection system.

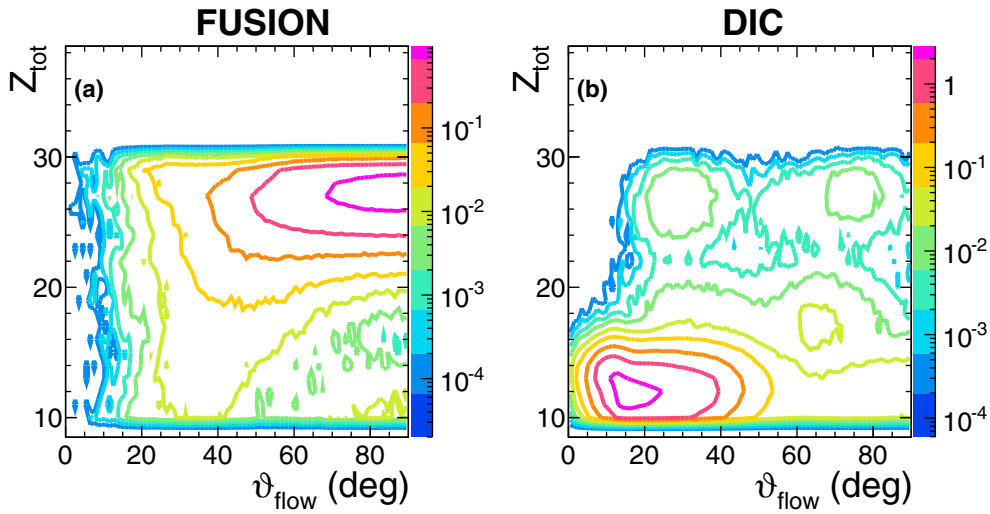

FIG. 6. Simulated contour plots of differential cross sections for the reaction $^{32}S + ^{48}Ca$ as a function of the ϑ_{flow} angle (binning: 1°) and of the total charge Z_{tot} (binning: 1 unit of charge). Calculations have been performed with the TWINGO code followed by GEMINI++ and the simulated events have been filtered by means of a software replica of the setup. (a) Events corresponding to fusion (both FE and FF); (b) events corresponding to DIC. The color scale indicated on the left is in units of mbarn/deg for each Z_{tot} value.

tensor of all the detected products. It is defined as the angle between the beam axis and the eigenvector corresponding to the largest eigenvalue of the tensor. Figure 6 shows the correlations obtained for filtered simulated events in the case of fusion [Fig. 6(a)] and in the case of DIC [Fig. 6(b)] for the reaction $^{32}S + ^{48}Ca$.

Fusion events (including FE and FF) shown in Fig. 6(a) are mainly located in the region of high Z_{tot} and $\vartheta_{flow} > 40°$; the weak tail extending below $Z_{tot} = 20$ is due to FF events in which one fission fragment is lost. The ϑ_{flow} distribution is broad and peaked around 90°. Even in the absence of the setup filter, this is expected because the data are presented as a function of ϑ_{flow} [and not of $\cos(\vartheta_{flow})$] and moreover our simulated primary fragment of $M = 1$ events (Fig. 3) has an average spin of 30 $\hbar$ (with a tail extending up to 60 $\hbar$).

On the contrary, the DIC events of Fig. 6(b) are mainly located in the region with $Z_{tot} < 20$ and $\vartheta_{flow} < 50°$, with a very pronounced peak around 20°. This is reasonable, because, on the one side, DIC events have an elongated shape with the main axis of the event quite close to the beam axis, and on the other side the QT is almost always lost, thus giving a reduced total detected charge. When both QP and QT are collected, we obtain the cloud of events at high Z_{tot} in Fig. 6(b). In the experimental case, where we cannot independently select the event type [as we did in the simulation to produce Figs. 6(a) and 6(b)], these events represent a background for the region where fusion events are mainly concentrated. In particular, the cloud at $\vartheta_{flow} < 40°$ corresponds to less dissipative events, while that beyond $\vartheta_{flow} = 60°$ to more dissipative events. This latter cloud includes also a small contribution of events in which only the QT is detected. On the basis of these results, we conclude that cuts on the correlation $(Z_{tot}, \vartheta_{flow})$ are well suited to separate the different reaction channels, with only minor cross contaminations.

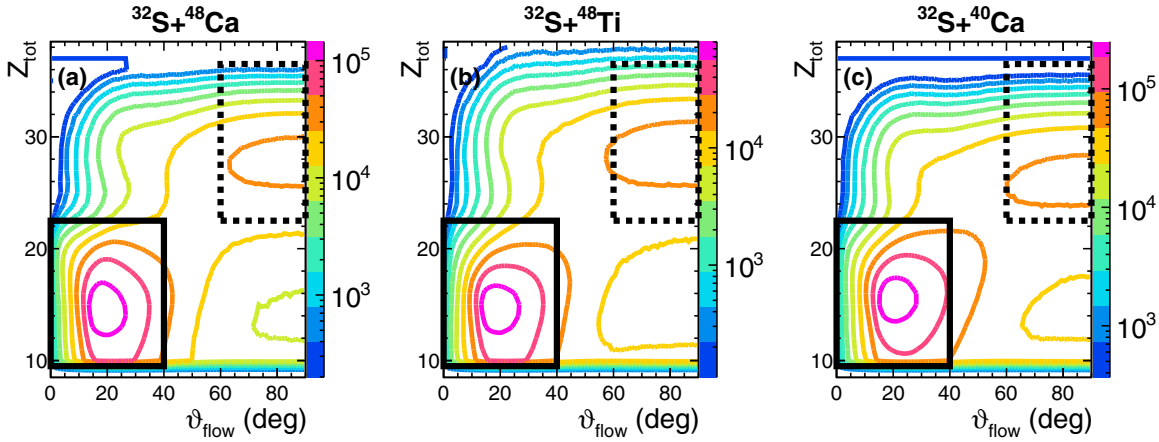

FIG. 7. Experimental contour plots as a function of the ϑ_{flow} angle and of the total charge Z_{tot}. (a) $^{32}S + ^{48}Ca$. (b) $^{32}S + ^{48}Ti$. (c) $^{32}S + ^{40}Ca$. The continuous black rectangle in the lower left corner corresponds to the adopted selection for DIC events ("DIC cut"), while the dotted black rectangle in the upper right corner corresponds to the adopted selection for FF and FE events ("fusion cut").

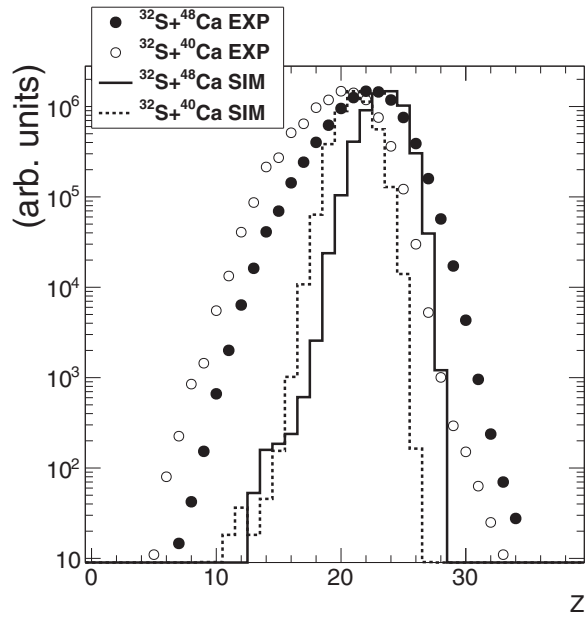

FIG. 8. Charge distribution of the ER in FE events. Symbols: experimental data (full circles: $^{32}S + ^{48}Ca$, open circles: $^{32}S + ^{40}Ca$). Lines: Simulated data produced by TWINGO followed by GEMINI++ as afterburner. Continuous line: $^{32}S + ^{48}Ca$, dotted line:$^{32}S + ^{40}Ca$. Data are normalized to the maximum, which corresponds, in the model calculation for $^{32}S + ^{48}Ca$, to 22.7 mbarn.

Figure 7 presents the experimental correlations $(Z_{tot}, \vartheta_{flow})$ for all the investigated reactions. The cuts adopted for the event selection are shown as black rectangles. The continuous one (lower left corner, hereafter "DIC cut") corresponds to the DIC selection for the events in which only the QP residue was detected. DIC events in which both QP and QT are detected are rare and they will not be considered from now on, also because they cannot be safely separated from FF events. In fact, as it was shown from the simulation [Fig. 6(b)], they are located in the upper part of the $(Z_{tot}, \vartheta_{flow})$ correlation, where they constitute a background for FF events, but not for FE events, because in this latter case only one heavy fragment is detected. Note that, on the contrary, the very small amount of cases in which the QT only is detected pollute the FE selection. Fusion events (FF and FE) are selected by the dotted rectangle (upper right corner, hereafter "fusion cut") shown in the picture; this cut excludes a minor part of fusion events, but it reduces in a substantial way the possible contamination of fully detected DIC events (QP and QT) within FF events.

1. *Fusion-evaporation events FE*

On the basis of the preceding discussion, in our analysis the FE condition means event inside the fusion cut of Fig. 7, with one and only one detected fragment ($Z > 3$) and with a reinforcing constraint on its velocity (c.m. velocity $v_{c.m.} < 15$ mm/ns).

The obtained charge distribution for the ER is shown in Fig. 8. Experimental data are shown as symbols (full circles for the reaction $^{32}S + ^{48}Ca$ and open circles for the reaction $^{32}S + ^{40}Ca$), while simulated data are plotted as lines. Two features are evident in this picture. First of all, when the target is ^{40}Ca, the ER charge distribution is shifted toward smaller Z values with respect to the case of the ^{48}Ca. This behavior is observed both for the experimental data and for the simulation. The average shift is equal in both cases and it amounts to about 2.2 charge units. This happens because the CN produced in the reaction $^{32}S + ^{40}Ca$ (^{72}Kr in the case of complete fusion) is sizably n deficient and hence it favors proton emission with respect to the case of the CN formed with the target of ^{48}Ca (^{80}Kr in case of complete fusion), which tends to emit more neutrons. The second striking point is the fact that the simulated distributions are narrower than the experimental ones. It seems that the secondary decay does not smear enough the ER charge distribution, suggesting that the excitation energy of the primary CN fed to the afterburner may be too small, even taking into account that the model has an uncertainty of about 0.5 MeV/nucleon on the excitation energy of the produced fragments.

The main reason for this discrepancy probably lies in the fact that the SMF model underestimates the dynamical fluctuations, which are only implemented in coordinate space [22,41]. As far as mean field approaches are concerned, the treatment of the fluctuations can be improved by implementing the Boltzmann-Langevin equation in full phase space, i.e., considering a stochastic collision integral, as done for instance in the recent Boltzmann-Langevin One Body model (BLOB) [41]. In this case, one would expect wider distributions for all physical observables. However, as a common limitation of mean field approaches, light cluster pre-equilibrium emission is not well described, because of the lack of explicit many-body correlations. This aspect is better accounted for in molecular-dynamics-like models. However, simulations performed with the antisymmetrized molecular dynamics (AMD) model (in the version of Ref. [34]) for the reactions under study gave an average charge of the ER that was too high, probably due to an underestimation of the nucleons emitted during the pre-equilibrium stage.

According to the model, the background of DIC events obtained with the adopted selection for the FE case is less than 0.2%; as it was already mentioned, it is due to events in which only the QT is detected. On the other side, a background of partially detected FF events (in which one of the fission partner is missing) cannot be excluded; this contribution may be responsible for the broad tail extending toward small Z values observed in the experimental charge distribution of the residue (open and full circles of Fig. 8).

2. *Fusion-fission events FF*

Among the events in the "fusion cut" of Fig. 7, those belonging to the FF class are recognized by requiring two detected fragments with $Z > 3$. Additional constraints on the c.m. relative velocity v_{rel} and c.m. relative angle $\vartheta_{rel}^{c.m.}$ of the two detected fragments are applied. In particular, v_{rel} must be in the range 20–35 mm/ns (compatible with the fission systematic description [45,46]) and $\vartheta_{rel}^{c.m.}$ must be greater than 120°. This adopted additional cut is shown as a black rectangle in Fig. 9, where the experimental correlation $\vartheta_{rel}^{c.m.}$ vs v_{rel} for the reaction $^{32}S + ^{48}Ca$ is shown for events belonging to the

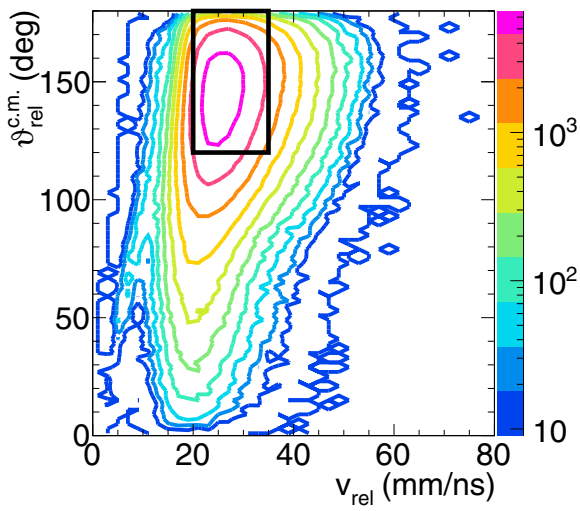

FIG. 9. Event distribution as a function of $\vartheta_{rel}^{c.m.}$ and v_{rel} for experimental data corresponding to the reaction $^{32}S + ^{48}Ca$, belonging to the fusion selection (inside the dotted rectangle of figure 7) and with two detected fragments with $Z > 3$. The black rectangle corresponds to the selection adopted for FF.

fusion selection (dotted cut of Fig. 7) and with two detected fragments. A clear and intense spot, corresponding to fission events, is evident in this correlation; this allows us to easily select a clean sample for this class of events. According to the model, about 8–10% of the so-identified FF events are actually strongly dissipative DIC events; this background cannot be practically removed because it populates almost the same phase space of FF events.

The $Z_1 + Z_2$ distribution (where $Z_1 + Z_2$ is the total charge of the pair of fission fragments) obtained after applying our FF selection is shown in Fig. 10 as open circles compared to the charge distribution of the ER found in FE events (full circles). Figure 10(a) refers to the reaction $^{32}S + ^{48}Ca$, and Fig. 10(b) refers to the reaction $^{32}S + ^{40}Ca$.

From this picture, it clearly emerges that the charge of the ER is on average lower than the sum of the charges of the two fission fragments. This behavior can be qualitatively explained

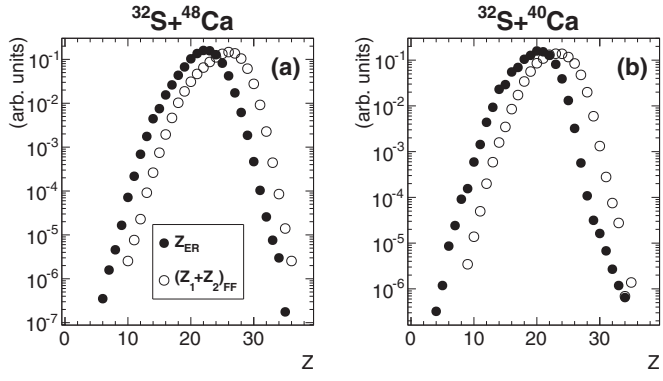

FIG. 10. Experimental distribution of charge Z of the ER (full circles) in FE events and of the total charge of the fragments $Z_1 + Z_2$ in FF events (open circles). (a) $^{32}S + ^{48}Ca$; (b) $^{32}S + ^{40}Ca$. Spectra are normalized to unitary area to better compare the distribution shapes.

by the fact that in a FF event a large amount of excitation energy is dissipated through the fission process, and thus the residual energy available for secondary decay is smaller. On the contrary, when a FE takes place, all the available excitation energy is dissipated through the evaporation of particles (and γ rays, not detected in this experiment), thus producing on average an ER with lower charge with respect to the total charge of the two fission fragments in a FF event.

The FE and FF channels will not be further discussed in this work, because they will be the subject of a forthcoming paper.

3. *Deep inelastic collision events*

As already mentioned, DIC events in which both QP and QT are detected are a minor part of our data and they have been discarded due to their large overlap with FF events. Only events where the QP alone is detected are retained in the further analysis by means of the DIC cut of Fig. 7, with some additional constraints suggested by the model (only one fragment with $Z = 8$–16 and c.m. emission angle lower than 60°). A lower threshold in the c.m. velocity of the fragment has been also required to exclude the most dissipative events. According to the model, the spurious contribution of fusion to these events is negligible (less than 0.005% in the worst case). However, in this event selection a much more important background arises from the scattering of the ^{32}S beam on the ^{12}C layers protecting the Ca targets against prompt oxidation. Such a contamination does not affect the fusion (FE and FF) selection thanks to the adopted lower threshold of $Z_{tot} > 22$ on the total detected charge (dotted gate of Fig. 7). On the contrary, FE reactions of the system $^{32}S + ^{12}C$ completely fulfill our DIC selection criteria when they are analyzed with the wrong kinematics (i.e., as if they came from $^{32}S + ^{40,48}Ca$), as we have verified with specific runs of $^{32}S + ^{12}C$ acquired during the experiment. As a result, the ^{12}C contribution to the DIC selection cannot be removed on an event-by-event basis. This contamination has to be removed on average by subtracting from all the relevant spectra those obtained in the runs of $^{32}S + ^{12}C$ analyzed as if they were $^{32}S + ^{40,48}Ca$, with a proper scaling factor. An estimate of such a scaling factor was obtained by comparing events with two detected fragments in the reactions $^{32}S + ^{12}C$ and $^{32}S + ^{40,48}Ca$, without any selection on the correlation between Z_{tot} and ϑ_{flow} (Fig. 7). Both systems were analyzed with the kinematics of the reaction $^{32}S + ^{40,48}Ca$ and the resulting correlations $\vartheta_{rel}^{c.m.}$ vs $Z_1 + Z_2$ are shown in Fig. 11(a) for $^{32}S + ^{48}Ca$ and in Fig. 11(b) for $^{32}S + ^{12}C$. In Fig. 11(a), two spots are evident: The upper one corresponds to FF from reactions on ^{48}Ca, and that inside the continuous areal gate (or the dotted one, for a more stringent selection) comes from FF in reactions on ^{12}C, as it is proved by the fact that the latter spot is evident also in Fig. 11(b), where the ^{12}C target is used. The elongated spot at $\vartheta_{rel}^{c.m.} > 70°$ in Fig. 11(b) corresponds to DIC reactions of $^{32}S + ^{12}C$. The fact that the corresponding structures in Figs. 11(a) and 11(b) come from the ^{12}C contribution is confirmed by the similarity of the projections on the $Z_1 + Z_2$ axis of the events inside the continuous (dotted) gate shown as continuous (dotted) curves in Fig. 11(c) for $^{32}S + ^{48}Ca$ (red curves) and for $^{32}S + ^{12}C$

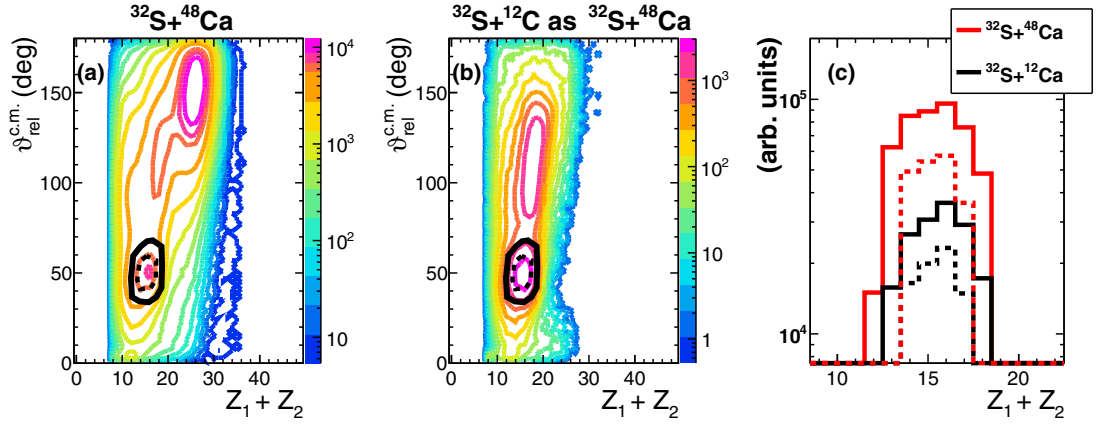

FIG. 11. (a) Distribution of experimental events, as a function of $\vartheta_{\rm rel}^{\rm c.m.}$ and of $Z_1 + Z_2$, associated to the detection of two fragments for the reaction $^{32}S + ^{48}Ca$. The inner black dotted gate is the region used to extract the ^{12}C background; the outer black continuous gate is another possible normalization region for the evaluation of the ^{12}C background. (b) The same for the reaction $^{32}S + ^{12}C$ analyzed as $^{32}S + ^{48}Ca$. (c) Projection on the $Z_1 + Z_2$ axis of part (a) (red lines) and part (b) (black lines) for the region inside the outer black continuous gate (continuous lines) and for the region inside the inner black dotted gate (dotted lines).

(black curves). The scaling factor is then obtained from the ratio of the number of events inside the dotted areal gates in Figs. 11(a) and 11(b). The systematic error associated with this procedure has been estimated by comparing the results obtained calculating the ratio which gives the scaling factors also from the events inside the outer continuous gates of Figs. 11(a) and 11(b).

A small ^{12}C contribution has been seen also in the reaction $^{32}S + ^{48}Ti$, where no ^{12}C protective layer is present. This is probably due to the C buildup on the target during the experiment that lasted several days, as expected for a vacuum level of 10^{-5} mbar.

The symbols in Fig. 12 show the experimental distributions of c.m. velocity [Fig. 12(a)] and charge [Fig. 12(b)] of the QP after subtracting the ^{12}C contribution for the three systems. All distributions are normalized to unitary area to better compare their shapes. The vertical dotted line in Fig. 12(b) corresponds to the chosen lower threshold for the QP charge. As it is evident from Fig. 12(a), where the arrow corresponds to the beam velocity, our DIC selection strongly suppresses peripheral reactions and this reflects in the QP charge distribution, which is shifted toward rather low values ($\langle Z \rangle = 11.1$). The charge distribution has an odd-even staggering behavior, as observed also in other experiments involving similar systems (e.g., $^{32}S + ^{58,64}$ Ni at 14.5 MeV/nucleon in Ref. [44]). The effect of the ^{12}C contamination can be appreciated by looking at the dotted line in Fig. 12(b), drawn before removing the ^{12}C background: The distribution is shifted to higher charge

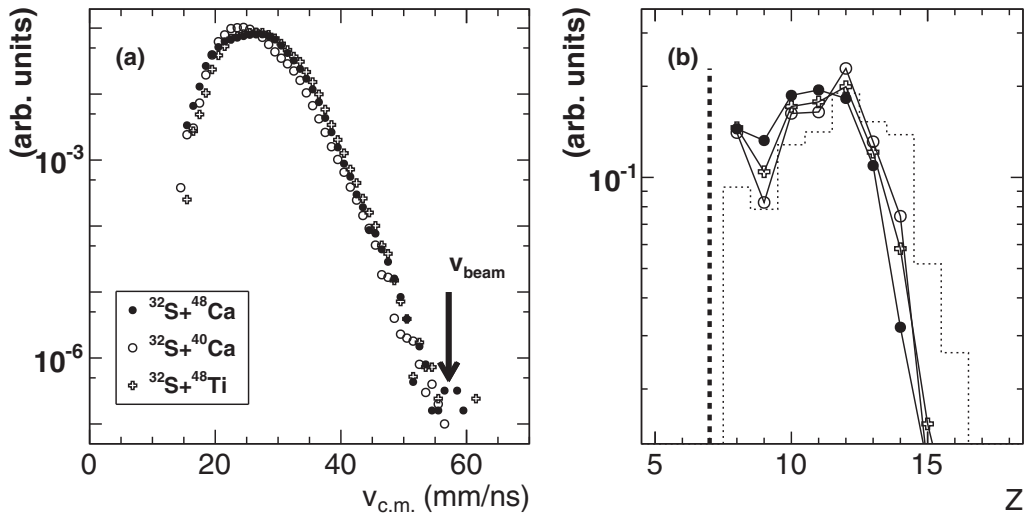

FIG. 12. (a) c.m. velocity distribution for the QP (normalized to 1) after subtracting the ^{12}C contribution for the three investigated reactions. The arrow corresponds to the beam velocity. (b) Charge distribution of the QP, normalized to 1, after subtracting the ^{12}C contribution. Full circles correspond to the reaction $^{32}S + ^{48}Ca$, open circles to $^{32}S + ^{40}Ca$, crosses to $^{32}S + ^{48}Ti$. The vertical dotted line shows the lower limit for the QP charge used in our analysis, while the dotted histogram corresponds to the charge distribution of the QP before ^{12}C subtraction for the reaction $^{32}S + ^{48}Ca$.

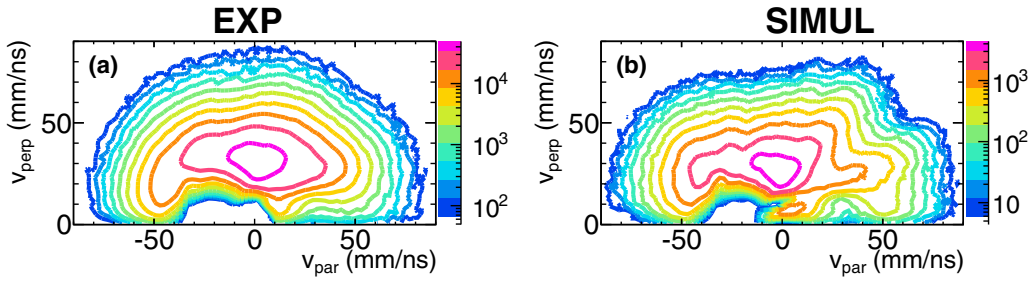

FIG. 13. Yields (arb. units) as a function of v_{perp} and v_{par} for protons emitted in DIC events for the reaction $^{32}S + ^{40}Ca$. (a) Experimental data after subtracting the ^{12}C contribution. (b) Simulated data (TWINGO followed by GEMINI++).

values because the ER from $^{32}S + ^{12}C$ reaction is erroneously interpreted as a QP from $^{32}S + ^{40,48}Ca$. From now on, all presented experimental data are shown after removing the ^{12}C background, except when otherwise specified. Although the details of the charge distribution are not reproduced by the adopted model (TWINGO followed by GEMINI++), it is worth noting that the experimental QP occupies the same charge range predicted by the model, thus further confirming the correctness of the chosen selection.

The v_{perp} vs v_{par} correlation for protons emitted in DIC events is shown in Fig. 13 for the reaction $^{32}S + ^{40}Ca$, both for experimental data and for the simulated ones. v_{perp} and v_{par} are, respectively, the perpendicular and parallel components of the c.m. velocity of the protons; these components are calculated with respect to the c.m. velocity of the QP. Simulated and experimental data qualitatively agree, although in the simulation all nucleons emitted by TWINGO before applying the afterburner are not included. In both panels, two sources, corresponding to QP and QT emission, can be approximately recognized, thus confirming the binary character of the selected events. As observed from Fig. 12, the measured DIC events are strongly dissipative and therefore the two QP-QT sources have a small relative velocity.

IV. RESULTS ON DIC CHANNEL

This section presents the obtained results on the isospin diffusion process, both for the experimental data and for the simulation.

A. Isospin diffusion: Experimental results

The effect of the isospin diffusion can be pointed out by comparing the average isospin of the QP as a function of its charge for the three investigated systems, i.e., when changing the target from ^{40}Ca, which has the same N/Z of the projectile, to ^{48}Ca, which is much more n rich than the projectile; the ^{48}Ti case is intermediate. If no diffusion took place, the isospin of the QP should be target independent, except for some minor effects due to the particle emission during the dynamical phase, which may alter the $\langle N\rangle/Z$ of the QP. It is worth noting that according to the model such dynamical emission is mainly of proton type for $^{32}S + ^{40}Ca$ and of neutron type for $^{32}S + ^{48}Ca$; therefore it tends to reduce the evidence of isospin diffusion. Figure 14 shows, for the three systems, the $\langle N\rangle/Z$ of the QP as a function of its charge Z. This observable is significantly dependent on the target and it is the highest for the n-rich ^{48}Ca and the lowest for the ^{40}Ca with the ^{48}Ti case in the middle. The effect is already evident when the original data are plotted (full symbols) and becomes even more pronounced after subtracting the ^{12}C background (open symbols). The correction for the undesired reaction $^{32}S + ^{12}C$, which is an isospin equilibrated one, is relevant only for the reaction on ^{48}Ca, while it is almost negligible for that on ^{40}Ca (isospin equilibrated system) and on ^{48}Ti (self-supporting target). The gray bands indicate the systematic errors on the subtraction procedure and they have been estimated comparing different recipes for the evaluation of the ^{12}C contribution (as an example, dotted and continuous gates in Fig. 11).

It is interesting to note that also in the ^{40}Ca case the $\langle N\rangle/Z$ of the QP is always above 1.0; as it was already cited, this fact may be due to the preferential emission of protons with respect to neutrons for this relatively n-poor system during both the dynamical and evaporative phase. Another observation about this picture is the fact that the difference in $\langle N\rangle/Z$ tends to increase when moving away from the projectile region ($Z = 16$), more for the ^{48}Ca, less for the ^{48}Ti, while the $\langle N\rangle/Z$

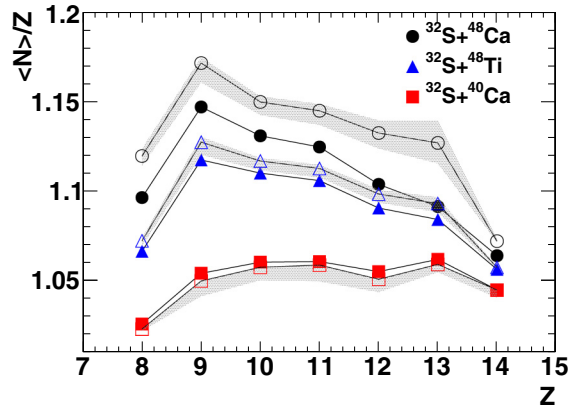

FIG. 14. Measured average $\langle N\rangle/Z$ of the QP as a function of its charge. Full (open) symbols (circles for $^{32}S + ^{48}Ca$, squares for $^{32}S + ^{40}Ca$, and triangles for $^{32}S + ^{48}Ti$) refer to the experimental data before (after) the subtraction of the ^{12}C background. Only statistical errors (smaller than the symbol size) are included for full symbols, while the gray band is the systematic error due to the ^{12}C subtraction procedure. Data refer only to QP detected in the ring counter through the Si-CsI(Tl) correlation, where information on the ion mass is available.

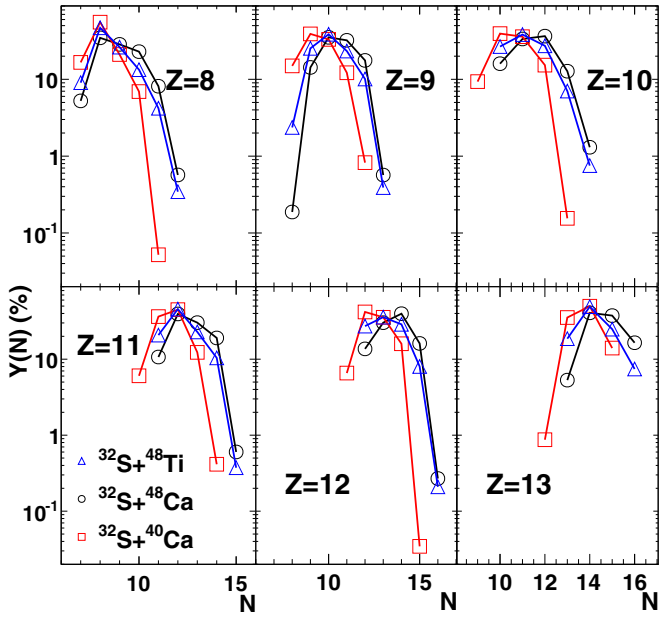

FIG. 15. Isotopic distribution (relative yields) of the QP after subtracting the ^{12}C background. Each panel refers to a different element. For $Z = 14$ (not shown in the figure), the N value ranges between 14 and 16 for $^{32}S + ^{48}Ca$ and $^{32}S + ^{48}Ti$ and between 13 and 16 for $^{32}S + ^{40}Ca$. Only statistical errors are shown.

remains almost constant for the ^{40}Ca target. This qualitatively corresponds to the fact that, when the dissipation increases, more nucleon exchanges occur and, due to the isospin diffusion process, the $\langle N\rangle/Z$ ratio tends to approach the equilibrium value, which is different for the three systems (see Table I).

The isotopic distributions from which the $\langle N\rangle/Z$ of the QP is built are shown as relative yields in Fig. 15 for the three systems. The shown data refer to the yields obtained after subtracting the ^{12}C background. The shift toward n-rich isotopes is clearly evident for the ^{48}Ca case. Another evidence of isospin diffusion can be obtained by comparing the isotopic ratios of particles emitted by the QP for the three systems. These ratios have been obtained from particles forward emitted—on an event-by-event basis—with respect to the QP. The isotopic ratios are observables rather robust with respect to geometrical corrections, because, at least to first approximation, the efficiency cuts are similar for the various species and almost identical for the three systems. The obtained results are presented in Table II for the three systems. We note that the effect of the ^{12}C background is critical for this observable and it is the main source of the very large systematic errors quoted in the table (statistical errors are negligible), evaluated comparing the results using different scaling factors for the ^{12}C subtraction, as mentioned in Sec. III C 3. Since the α emission in the $^{32}S + ^{12}C$ reaction is quite relevant and very difficult to reliably correct for, in Table II we present only ratios of hydrogen isotopes. We gave also a look at the isotopic/isobaric ratios for Li and Be forward emitted with respect to the QP, both for the Ca targets and the C one. We found that the majority of Li and Be observed for the Ca targets must be attributed to the C background; as a consequence we were not able to give a trustworthy estimate of the ratios involving light fragments. The fact that the QP evaporates few Li and Be is not surprising, even more so because it is a small QP (S-like) and with smaller excitation energy with respect to a CN of fusion events. On the contrary, the CN of S+C (a Ti-like nucleus) has more chances to evaporate a small fragment. By the way, also in a heavier system as the one discussed in Ref. [47] ($^{93}Nb + ^{93}Nb$ at 17 MeV/nucleon), the amount of evaporated fragments from the QP in semiperipheral collisions is less than 50% of the total fragment multiplicity (the largest part of the emission comes from the midvelocity mechanism).

TABLE II. Experimental isotopic ratios for forward-emitted particles with respect to the QP in DIC events. Only systematic errors due to the subtraction procedure are shown, since they are much larger than the statistical ones.

Reaction	d/p	t/p
$^{32}S + ^{40}Ca$	0.064 ± 0.004	0.007 ± 0.001
$^{32}S + ^{48}Ti$	0.114 ± 0.005	0.027 ± 0.003
$^{32}S + ^{48}Ca$	0.19 ± 0.04	0.07 ± 0.02

Within the error limits, the shown data concerning H isotopes confirm the neutron enrichment of the QP emission when the N/Z of the target increases. It is worthwhile to note that this effect is observed for whatever scaling factor for the subtraction of the ^{12}C background is adopted and it is observed also in the original data before subtraction.

A quite similar behavior for reactions at intermediate beam energies was observed, for example, in Ref. [48], where the isospin ratio of light charged products emitted by the QP was found to increase with increasing the N/Z of the target.

B. Isospin diffusion: Simulated data

The $\langle N\rangle/Z$ of the QP for the two systems $^{32}S + ^{40}Ca$ and $^{32}S + ^{48}Ca$ can be investigated also for simulated data. For primary data (i.e., before applying the afterburner), a net effect of isospin diffusion is found, as shown in Fig. 16(a). The TWINGO code has been run using both the asystiff parametrization for the symmetry energy term of the EOS, full (open) crosses for ^{48}Ca (^{40}Ca), and the asysoft one, here shown only for the ^{48}Ca case as open diamonds [24]. We observe a constant $\langle N\rangle/Z$ value for the ^{40}Ca case as a function of the impact parameter because the interacting nuclei have the same initial $N/Z = 1$. At variance, in the case of ^{48}Ca charge equilibration takes place and the $\langle N\rangle/Z$ of the QP moves from a value equal to the ^{40}Ca case for peripheral collisions (where a limited nucleon exchange takes place) toward the N/Z value of the total system (1.22) when the impact parameter decreases, i.e., when the nucleon exchange process becomes more effective. We observe also that the $\langle N\rangle/Z$ value for the most peripheral collisions (and for all impact parameters in $^{32}S + ^{40}Ca$) is slightly larger than expected (1.06 instead of 1.0 which is the value of ^{32}S). This effect is due to the spurious emission of test particles also in very peripheral collisions. The fact that the QP sources are n deficient favors a preferential emission of proton-type particles, thus increasing the N/Z. The observed value of 1.06 corresponds to the fast

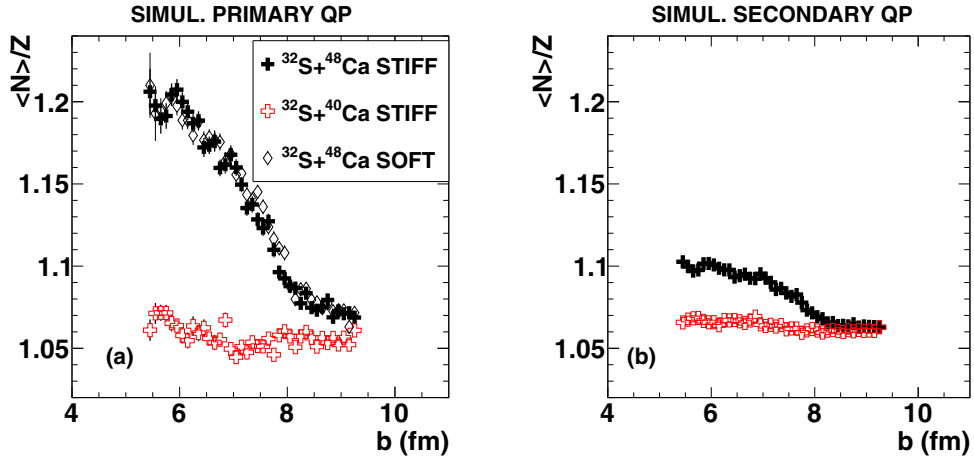

FIG. 16. Simulated data, $\langle N\rangle/Z$ of the QP as a function of the impact parameter. (a) primary data (TWINGO only). (b) secondary data (TWINGO plus GEMINI++), not filtered with the software replica of the experimental setup. Full crosses: $^{32}\mathrm{S}+^{48}\mathrm{Ca}$ with asystiff parametrization for the symmetry energy term; open diamonds [only in part (a)]: $^{32}\mathrm{S}+^{48}\mathrm{Ca}$ with asysoft parametrization. Open crosses: $^{32}\mathrm{S}+^{40}\mathrm{Ca}$ with asystiff parametrization.

emission of just one proton (and no neutron) from the QP. No differences have been found when the symmetry energy parametrization is changed from asystiff to asysoft. This means that at these beam energies during the dynamical phase the system explores only regions close to the normal density, where both parametrizations are equal.

The application of the afterburner partially blurs the isospin diffusion effect, as shown in Fig. 16(b). The difference in $\langle N\rangle/Z$ between the neutron-rich and neutron-poor cases is reduced, although a residual effect is still clearly recognizable. Obviously, the resulting effect depends not only on the dynamical model describing the reaction but also on the details of the evaporation code. The fine-tuning of the decay model parameters to reproduce the experimental data is a very delicate task and is beyond the scope of this work.

From the experimental point of view, the impact parameter is not directly accessible. Therefore, we prefer to present the $\langle N\rangle/Z$ of the QP as a function of its charge, as done in the experimental case, although we have previously checked that the correlation $Z_{\mathrm{QP}} - b$ is rather weak and broad even for primary fragments, as it is shown in Fig. 17. Of course, we cannot exclude that a very marginal mixing between QP and QT takes place for the most dissipative impact parameters.

The $\langle N\rangle/Z$ for the QP as a function of its charge is plotted in Figs. 18(a) and 18(b) for primary and secondary fragments, respectively. The corresponding charge distributions for primary and secondary fragments are shown in Figs. 18(c) and 18(d), respectively. For primary fragments of ^{48}Ca, results obtained with both the asystiff and the asysoft parametrization are shown and, again, they are almost indistinguishable. Concerning the QP charge, the slight difference between the ^{48}Ca case and the ^{40}Ca one observed for primary distributions [Fig. 18(c)] is reduced by the evaporation, so that the charge distributions of cold fragments are almost identical for the two systems [Fig. 18(d)]. As expected, the charge distributions are shifted to lower values, with larger production of light fragments representing the stop points of the cascades for most excited QP.

Concerning the QP $\langle N\rangle/Z$ vs Z, for primary fragments [Fig. 18(a)] a clear isospin diffusion effect is observed for small Z, i.e., in dissipative collisions (see Fig. 17), in qualitative agreement with the results of Fig. 16(a). For peripheral collisions, mostly giving large QP charges, we find a common $\langle N\rangle/Z$ value for both systems, because the nucleon exchange is small and QP fragments keep strong memory of the initial $N/Z = 1$.

The secondary decay strongly reduces the evidence of isospin diffusion [Fig. 18(b)]. In this case, since the correlation between the charge of the QP and the impact parameter is even weaker than for primary fragments, the evidence is further reduced with respect to Fig. 16(b), where data were presented as a function of the impact parameter. A

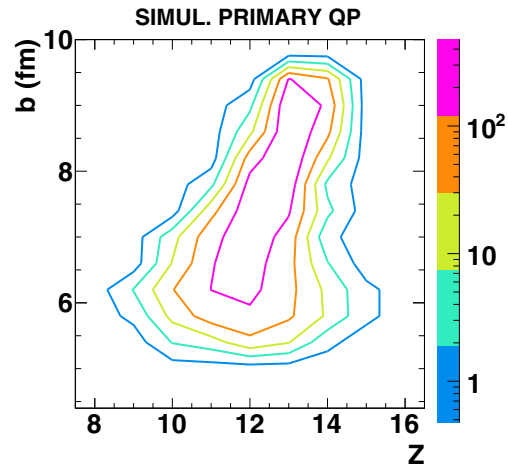

FIG. 17. TWINGO simulation, primary data. Event distribution as a function of the impact parameter b and the charge Z of the QP for the reaction $^{32}\mathrm{S}+^{48}\mathrm{Ca}$ with asystiff parametrization. The color scale gives the differential cross section $d\sigma/db$ in units of mbarn/fm for each Z value; the binning of the abscissa is 1 unit of charge, while the binning of the ordinate is 0.4 fm.

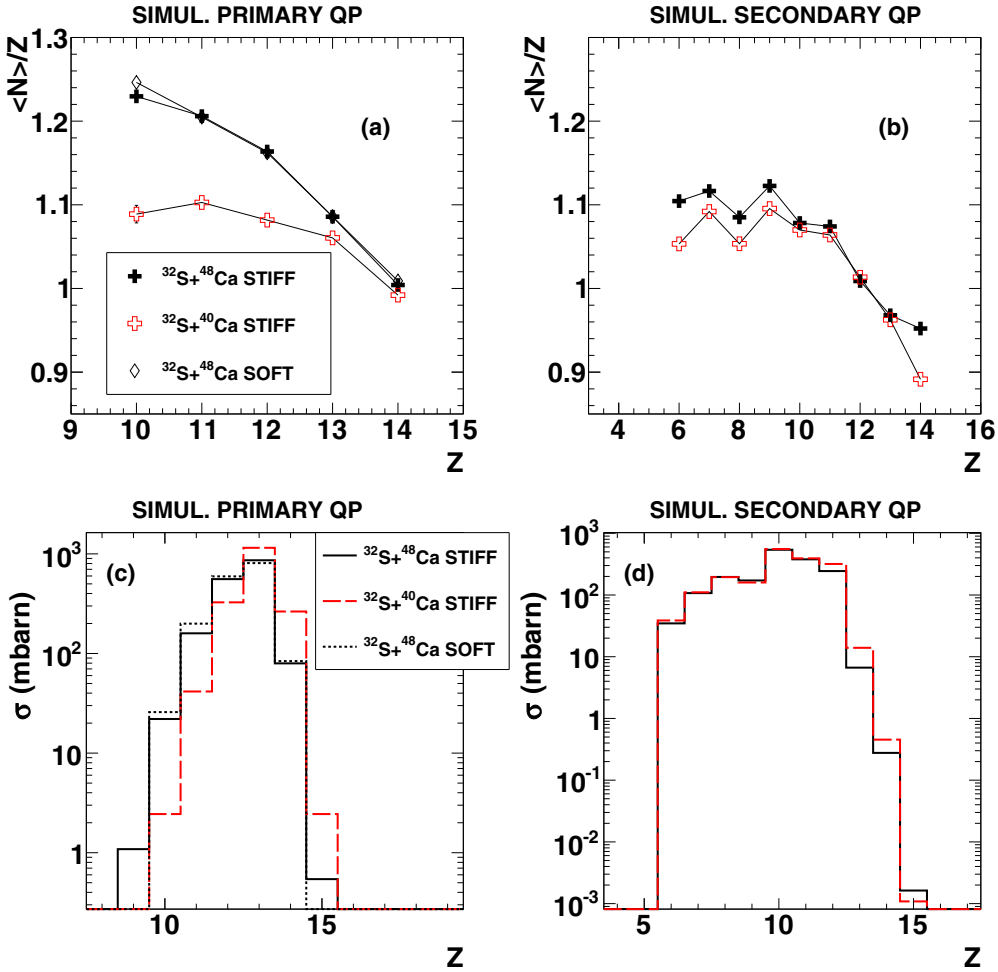

FIG. 18. Simulated data. Parts (a) and (b): $\langle N\rangle/Z$ for the QP as a function of its charge for primary (TWINGO only) and secondary data (TWINGO followed by GEMINI++ as afterburner, not filtered with the software replica of the experimental setup), respectively. Full crosses [open diamonds in part (a) only]: ^{32}S + ^{48}Ca with asystiff (asysoft) parametrization for the symmetry energy term. Open crosses: ^{32}S + ^{40}Ca with asystiff parametrization. Parts (c) and (d): cross section as a function of the charge Z of the QP for primary and secondary data (not filtered with the software replica of the experimental setup), respectively. Full [dotted in part (c) only] black line: ^{32}S + ^{48}Ca with asystiff (asysoft) parametrization for the symmetry energy term. Dashed red line: ^{32}S + ^{40}Ca with asystiff parametrization. The binning of the abscissa is 1 unit of charge.

marginal effect survives only for small charge values, while in the experimental case (Fig. 14) the difference between the neutron-rich and the neutron-poor cases is evident for all the charge values, with a decrease of the gap towards higher Z, i.e., for more peripheral collisions. This discrepancy may be due to the interplay of the dynamical and of the statistical decay models. For example, within the TWINGO code, the uncertainty on the excitation energy of the primary fragments is around 0.5 MeV/nucleon. By reducing the excitation energy of the fragments of such an amount (namely, primary fragments are assumed to be less excited), we restore part of the isospin difference for the secondary fragments, which anyhow remains less than the measured one.

A direct comparison between experimental and simulated data is shown in Fig. 19, where for the experimental case only ^{12}C-subtracted data are shown and for the simulation the obtained events have been filtered by means of the software replica of the setup.

As already discussed, a detailed reproduction of the measured effect is not within the scope of this work, and it would require a fine-tuning of the afterburner coupled with the dynamical code. Two points are worth noting: First, at these beam energies it is not possible to extract usable information on the stiffness of the symmetry energy term from the $\langle N\rangle/Z$ ratios. Second, the model predicts some isospin diffusion, as observed also in the experimental data, namely, a larger $\langle N\rangle/Z$ ratio for the reaction with the ^{48}Ca target. However, we notice an overestimation (underestimation) of the data for the ^{40}Ca (^{48}Ca) case, by about 4% (6%), up to $Z = 11$. This might be attributed to an overestimation of the neutron (proton) pre-equilibrium emission, for the neutron-rich (proton-rich) system or to the treatment of the secondary decay process by GEMINI++. The steep decrease of the $\langle N\rangle/Z$ observed in the simulation for $Z = 12-13$ can be ascribed to spurious nucleon emission in peripheral reactions, whose description, as stressed above, would require a higher numerical accuracy.

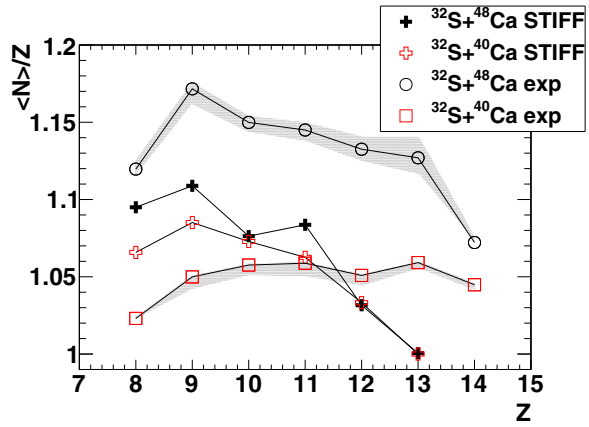

FIG. 19. $\langle N\rangle/Z$ for the QP as a function of its charge. Open circles and open squares: experimental data after subtracting the ^{12}C background (the gray area corresponds to the systematic error associated to the subtraction procedure). Crosses: simulation, secondary data (TWINGO followed by GEMINI++), filtered by means of the software replica of the setup.

Indeed, $\langle N\rangle/Z$ around 1 should correspond to the charge of the projectile.

These findings are much in line with the results of Ref. [49], where the reactions ^{58}Ni + ^{58}Ni, ^{197}Au were measured at Fermi energies in the range 52–74 MeV/nucleon and then simulated by means of the TWINGO code followed by SIMON [50] as afterburner. Concerning the first point mentioned above, the authors of Ref. [49] found that there is only a small difference in the predicted average isospin of the primary QP when the asystiff and the asysoft parametrizations for the symmetry energy term are compared. All the more, it is not surprising that our data are so little sensitive to the adopted stiffness, since at these low energies the system remains very close to the normal density ρ_0. Concerning the second point, in Ref. [49] a clear effect of isospin diffusion, larger for less peripheral collisions, was found in the simulated data by comparing the isospin ratio of the primary QP when the target changes from ^{58}Ni to ^{197}Au, as it happens also in our case. Moreover, the secondary decay from the hot fragments was found to narrow the difference in the QP isospin ratio calculated for the two different targets (in that case, extracted from the isospin of the complex particles emitted by the QP), again as it happens in our case, thus reducing the sensitivity of $\langle N\rangle/Z$ on the details of the nucleon exchange process.

V. SUMMARY AND CONCLUSIONS

In this work, an experimental study of the systems ^{32}S + ^{40,48}Ca and ^{32}S + ^{48}Ti at 17.7 MeV/nucleon was presented. Experimental data were collected with the GARFIELD plus ring counter setup [25] at LNL of INFN. The good angular coverage (66% of the full solid angle and 70% of the forward hemisphere) allowed us to measure with high efficiency the isotopic composition of the LCP at all polar angles. Fragments with charge up to $Z = 14$ were also isotopically resolved, provided that they were detected in the angular range 5.4°–17.0° and that they punched through the 300-μm Si layer. Heavier fragments as well as fragments emitted beyond 17° were only resolved in charge.

Three main classes of events were identified in the collected data: FE (fusion evaporation), FF (fusion fission), and DIC (deep inelastic collisions). The selection criteria were verified with a simulation based on a dynamical model (SMF [29]) followed by an afterburner (GEMINI++ [30]). FE and FF events will be the subject of a forthcoming paper, while this work focuses on DIC events. In particular, the isospin transport phenomenon was pointed out by comparing the $\langle N\rangle/Z$ of the QP in reactions with different targets: We found that QPs from the reaction on ^{48}Ca are systematically more neutron rich than those from the reaction on ^{40}Ca and this effect increases for more dissipative collisions. Simulated data predict a similar trend for primary fragments, but the decay process strongly reduces the effect, which becomes definitely smaller than the measured one. No appreciable difference in the average isospin of the QP is found when changing the parametrization of the symmetry energy term from asystiff to asysoft. This is not surprising, because in this energy regime the system does not explore density regions far from the normal value, where both parametrizations coincide. To our knowledge, this is the first direct experimental evidence of isospin enrichment of the QP for nearly symmetric systems at the same time as light as ours and at energies similar to that of the present study.

Finally, in the experimental case the isospin equilibration process has been also studied by looking at the hydrogen isotopic ratio. Within the error limits, the experimental d/p and t/p ratios were found to increase when the isospin of the target increases. This effect indicates a neutron enrichment of the QP, coherently with the direct observation of the QP isotopic population and in agreement with other experimental studies. This gives further evidence for isospin diffusion between target and projectile, as shown also in Ref. [48] for a heavier system at higher energies.

ACKNOWLEDGMENTS

Thanks are due to the accelerator staff of Legnaro Laboratories for having provided good-quality beams and to the Target Lab of INFN-LNL and INFN-LNS for providing the targets used during this experiment. This work was partially supported by grants from the Italian Ministry of Education, University, and Research under Contract PRIN 2010-2011. This project has received funding from the European Unions Horizon 2020 research and innovation programme under Grant Agreement No. 654002.

[1] M. T. Magda, E. Bauge, A. Elmaani, T. Braunstein, C. J. Gelderloos, N. N. Ajitanand, J. M. Alexander, T. Ethvignot, P. Bier, L. Kowalski *et al.*, Phys. Rev. C **53**, R1473(R) (1996).

[2] L. Lassen, P. von Neumann-Cosel, A. Oberstedt, and G. Schrieder, Phys. Rev. C **55**, 1900 (1997).

[3] M. Di Toro, V. Baran, M. Colonna, and V. Greco, J. Phys. G: Nucl. Part. Phys. **37**, 083101 (2010).
[4] H. Breuer, B. G. Glagola, V. E. Viola, K. L. Wolf, A. C. Mignerey, J. R. Birkelund, D. Hilscher, A. D. Hoover, J. R. Huizenga, W. U. Schröder, and W. W. Wilcke, Phys. Rev. Lett. **43**, 191 (1979).
[5] G. J. Balster, P. C. N. Crouzen, P. B. Goldhoorn, R. H. Siemssen, and H. W. Wilschut, Nucl. Phys. A **468**, 93 (1987).
[6] G. J. Balster, H. W. Wilschut, R. H. Siemssen, P. C. N. Crouzen, P. B. Goldhoorn, and Z. Sujkowski, Nucl. Phys. A **468**, 131 (1987).
[7] H. Freiesleben and J. Kratz, Phys. Rep. **106**, 1 (1984).
[8] S. J. Asztalos, I. Y. Lee, K. Vetter, B. Cederwall, R. M. Clark, M. A. Deleplanque, R. M. Diamond, P. Fallon, K. Jing, L. Phair *et al.*, Phys. Rev. C **61**, 014602 (1999).
[9] S. Bottoni, G. Benzoni, S. Leoni, D. Montanari, A. Bracco, F. Azaiez, S. Franchoo, I. Stefan, N. Blasi, F. Camera *et al.*, Phys. Rev. C **85**, 064621 (2012).
[10] G. Benzoni, F. Azaiez, G. I. Stefan, S. Franchoo, S. Battacharyya, R. Borcea, A. Bracco, L. Corradi, D. Curien, G. De France *et al.*, Eur. Phys. J. A **45**, 287 (2010).
[11] L. Corradi, G. Pollarolo, and S. Szilner, J. Phys. G: Nucl. Part. Phys. **36**, 113101 (2009).
[12] G. A. Souliotis, M. Veselsky, S. Galanopoulos, M. Jandel, Z. Kohley, L. W. May, D. V. Shetty, B. C. Stein, and S. J. Yennello, Phys. Rev. C **84**, 064607 (2011).
[13] M. Veselsky and G. A. Souliotis, Nucl. Phys. A **872**, 1 (2011).
[14] I. Lombardo, C. Agodi, R. Alba, F. Amorini, A. Anzalone, I. Berceanu, G. Cardella, S. Cavallaro, M. B. Chatterjee, E. De Filippo *et al.*, Phys. Rev. C **82**, 014608 (2010).
[15] M. B. Tsang, Y. Zhang, P. Danielewicz, M. Famiano, Z. Li, W. G. Lynch, and A. W. Steiner, Phys. Rev. Lett. **102**, 122701 (2009).
[16] K. Brown, S. Hudan, R. T. deSouza, J. Gauthier, R. Roy, D. V. Shetty, G. A. Souliotis, and S. J. Yennello, Phys. Rev. C **87**, 061601 (2013).
[17] S. Barlini, S. Piantelli, G. Casini, P. R. Maurenzig, A. Olmi, M. Bini, S. Carboni, G. Pasquali, G. Poggi, A. A. Stefanini *et al.* (FAZIA Collaboration), Phys. Rev. C **87**, 054607 (2013).
[18] E. De Filippo, A. Pagano, P. Russotto, F. Amorini, A. Anzalone, L. Auditore, V. Baran, I. Berceanu, B. Borderie, R. Bougault *et al.*, Phys. Rev. C **86**, 014610 (2012).
[19] R. E. Tribble, R. H. Burch, and C. A. Gagliardi, Nucl. Instrum. Methods Phys. Res., Sect. A **285**, 441 (1989).
[20] D. Shapira, J. Gomez del Campo, M. Korolija, J. Shea, C. F. Maguire, and E. Chavez-Lomeli, Phys. Rev. C **55**, 2448 (1997).
[21] C. Rizzo, M. Colonna, V. Baran, and M. Di Toro, Phys. Rev. C **90**, 054618 (2014).
[22] M. Colonna, M. Di Toro, A. Guarnera, S. Maccarone, M. Zielinska-Pfabe, and H. H. Wolter, Nucl. Phys. A **642**, 449 (1998).
[23] T. Skyrme, Nucl. Phys. **9**, 615 (1958–1959).
[24] V. Baran, M. Colonna, V. Greco, and M. Di Toro, Phys. Rep. **410**, 335 (2005).
[25] M. Bruno, F. Gramegna, T. Marchi, L. Morelli, G. Pasquali, G. Casini, U. Abbondanno, G. Baiocco, L. Bardelli, S. Barlini *et al.*, Eur. Phys. J. A **49**, 128 (2013).
[26] N. Le Neindre, R. Bougault, S. Barlini, E. Bonnet, B. Borderie, G. Casini, A. Chbihi, P. Edelbruck, J. D. Frankland, D. Gruyer *et al.*, Nucl. Instrum. Methods Phys. Res., Sect. A **701**, 145 (2013).
[27] A. J. Sierk, Phys. Rev. C **33**, 2039 (1986).
[28] S. K. Gupta and S. Kailas, Z. Phys. A **317**, 75 (1984).
[29] A. Guarnera, M. Colonna, and Ph. Chomaz, Phys. Lett. B **373**, 267 (1996).
[30] R. J. Charity, Phys. Rev. C **82**, 014610 (2010).
[31] J. Aichelin, Phys. Rep. **202**, 233 (1991).
[32] J. Lukasik and Z. Majka, Acta Phys. Pol. B **24**, 1959 (1993).
[33] A. Ono, H. Horiuchi, T. Maruyama, and A. Ohnishi, Phys. Rev. Lett. **68**, 2898 (1992).
[34] A. Ono, J. Phys.: Conf. Ser. **420**, 012103 (2013).
[35] M. Papa, G. Giuliani, and A. Bonasera, J. Comput. Phys. **208**, 403 (2005).
[36] L. Shvedov, M. Colonna, and M. Di Toro, Phys. Rev. C **81**, 054605 (2010).
[37] V. Zagrebaev and W. Greiner, J. Phys. G: Nucl. Part. Phys. **31**, 825 (2005).
[38] L. Tassan-Got and C. Stephan, Nucl. Phys. A **524**, 121 (1991).
[39] D. Lacroix, A. Van Lauwe, and D. Durand, Phys. Rev. C **69**, 054604 (2004).
[40] S. A. Kalandarov, G. G. Adamian, N. V. Antonenko, and W. Scheid, Phys. Rev. C **82**, 044603 (2010).
[41] P. Napolitani and M. Colonna, Phys. Lett. B **726**, 382 (2013).
[42] A. Bonasera, F. Gulminelli, and J. Molitoris, Phys. Rep. **243**, 1 (1994).
[43] S. Valdré, S. Piantelli, G. Casini, S. Barlini, S. Carboni, M. Ciemala, M. Kmiecik, A. Maj, K. Mazurek, M. Cinausero *et al.*, Phys. Rev. C **93**, 034617 (2016).
[44] M. D'Agostino, M. Bruno, F. Gulminelli, L. Morelli, G. Baiocco, L. Bardelli, S. Barlini, F. Cannata, G. Casini, E. Geraci *et al.*, Nucl. Phys. A **861**, 47 (2011).
[45] V. E. Viola Jr., Nucl. Data Sheets **1**, 391 (1965).
[46] V. E. Viola, K. Kwiatkowski, and M. Walker, Phys. Rev. C **31**, 1550 (1985).
[47] S. Piantelli, P. R. Maurenzig, A. Olmi, L. Bardelli, A. Bartoli, M. Bini, G. Casini, C. Coppi, A. Mangiarotti, G. Pasquali, G. Poggi, A. A. Stefanini, N. Taccetti, and E. Vanzi, Phys. Rev. C **74**, 034609 (2006).
[48] E. Galichet, M. F. Rivet, B. Borderie, M. Colonna, R. Bougault, A. Chbihi, R. Dayras, D. Durand, J. D. Frankland, D. C. R. Guinet *et al.* (INDRA Collaboration), Phys. Rev. C **79**, 064614 (2009).
[49] E. Galichet, M. Colonna, B. Borderie, and M. F. Rivet, Phys. Rev. C **79**, 064615 (2009).
[50] D. Durand, Nucl. Phys. A **541**, 266 (1992).